Fundamental Research 2 (2022) 937–945

Contents lists available at ScienceDirect

Fundamental Research

journal homepage: http://www.keaipublishing.com/en/journals/fundamental-research/

Article

Electroreduction of carbon dioxide to multi-electron reduction products using poly(ionic liquid)-based Cu-Pd catalyst

Xiao-Qiang Li[a,b], Guo-Yi Duan[a], Xian-Xia Yang[c], Li-Jun Han[a], Bao-Hua Xu[a,b,*]

[a] Beijing Key Laboratory of Ionic Liquids Clean Process, CAS Key Laboratory of Green Process and Engineering, State Key Laboratory of Multiphase Complex Systems, Institute of Process Engineering, Chinese Academy of Sciences, Beijing 100190, China
[b] School of Chemical Engineering, University of Chinese Academy of Sciences, Beijing 100049, China
[c] National Fundamental Research Laboratory of New Hazardous Chemicals Assessment and Accident Analysis, Institute of Applied Electrochemistry, Beijing University of Chemical Technology, Beijing 100029, China

ARTICLE INFO

Article history:
Received 30 August 2021
Received in revised form 18 December 2021
Accepted 21 December 2021
Available online 1 January 2022

Keywords:
CO_2 conversion
Bimetallic catalyst
Cu-Pd material
Electrolysis
High-value products

ABSTRACT

Electrocatalytic reduction of CO_2 (CO_2RR) to multi-electron (> $2e^-$) products provides a green and sustainable route for producing fuels and chemicals. Introducing the second metal element is a feasible strategy for "managing" the key intermediate on Cu-based materials to further improve the CO_2RR catalytic performance. In this work, palladium, which promises the generation of CO, was introduced into the poly(ionic liquid)-based copper hybrid (Cu@PIL) to construct a novel Cu-Pd bimetallic electrocatalyst (Cu@PIL@Pd). Remarkably, with a small dosage of palladium (2.0 mol% compared with Cu), a high faradaic efficiency (FE) for C_{2+} products (68.7%) was achieved at –1.01 V (with respect to the reversible hydrogen electrode (RHE), the same below) with a high partial current density of 178.3 mA cm^{-2}. Meanwhile, high selectivity towards CH_4 (FE = 42.5%) and corresponding partial current density of 172.8 mA cm^{-2} were obtained on the same catalyst at –1.24 V, signifying a significant potential-dependent selectivity. Mechanistic studies reveal that both copper and palladium oxides are reduced to metallic states during the CO_2RR. The presence of the adjoint copper phase and the highly dispersed electrostatic layer promote the generation of CO on the palladium components (both the PdO_2 phase and the Pd(II) site). Besides, the local CO* was enriched by the significant diffusion resistance of CO in the PIL layer. The spillover of CO* from Pd sites to the adjoint Cu sites, accompanied by the increased local concentration of CO* around Cu sites, accounted for the observed good CO_2RR catalytic performance, especially the high C_{2+} product selectivity.

1. Introduction

Electrocatalytic reduction of carbon dioxide (CO_2RR) has drawn much attention in the scientific community owing to its potential to convert CO_2 into valuable products by using renewable energies under mild conditions [1–5], which is of great importance for sustainable development [5,6]. To date, a variety of metals, including noble metals (e.g., Pd, Au, and Ag) [7,8] and non-noble metals (e.g., Cu, Zn, In, Sn, and Bi) [9], have been demonstrated to possess the electrocatalytic activity of CO_2RR. Copper-based materials, on which high-value multi-electron (more than 2 electrons) reduction products, such as methane (CH_4), ethylene (C_2H_4), acetic acid (HOAc), methanol (MeOH), ethanol (EtOH), and propanol (PrOH), could be generated, have aroused great interest [10,11]. Apart from an opportune affinity for the key CO* intermediate, the ability to promote the C–C coupling reaction accounts for the distinct property of copper-based materials for the CO_2RR [12–14].

In order to further improve the electrocatalytic performance of copper-based materials, various catalyst design strategies, including surface modification [15], defects engineering [16], electronic structure regulation [17], morphology control [18], and intermediate management [17,19], have been employed. Among them, introducing the second metal element was found to increase the local concentration of CO* intermediate on the Cu sites, thus promoting the CO_2RR performance [20]. Palladium, which is beneficial to producing CO [21–23], is regarded as a promising metal for constructing the binary electrocatalysts for CO_2RR [24–28]. For example, Ma et al. prepared a series of Cu-Pd catalysts with well-defined mixing patterns and found that the faradaic efficiencies of C_{2+} products (FE_{C2+} = 63%) on Cu-Pd catalysts with phase-separated atomic arrangements were much higher than those on order and disordered Cu-Pd catalysts [24]. Further, by modifying tetrahexahedral Pd nanocrystals possessing high-index facets with Cu overlayer, high selectivity towards alcohols ($FE_{MeOH + EtOH}$ = 20.4%) could be achieved [25]. Feng et al. reported that a high FE of C_2H_4 (FE_{C2H4} = 45.2%) was obtained on a Cu-Pd bimetallic catalyst, which was prepared by an electrodeposition method [26]. Zhu et al. found that the Cu-Pd interface could lower the barrier for the C–C coupling reaction, which resulted in a high FE_{C2+} of 50.3% on the CuPd(100) cata-

* Corresponding author.
E-mail address: bhxu@ipe.ac.cn (B.-H. Xu).

https://doi.org/10.1016/j.fmre.2021.12.009

lyst [27]. Lyu et al. employed Pd-Cu Janus nanocrystal with a controlled shape as an electrocatalyst, which provided a high FE_{C2+} of 51.0% [28]. In the study, they demonstrated that the high CO coverage on Pd atoms facilitated the C−C coupling reaction on the adjoint Cu atoms, thus improving the selectivity to C_{2+} products.

Despite the encouraging results achieved on Cu-Pd bimetallic catalysts, the performance still has room for improvement as demonstrated by the following three aspects: (i) further improving the selectivity towards the high-value multi-electron reduction products, especially the C_{2+} products; (ii) promoting the CO_2RR experiments at industrial current density (> 100 mA cm^{-2}); (iii) reducing the cost of catalyst by decreasing the dosage of noble-metal palladium [7]. Most recently, our group documented a novel Cu-poly(ionic liquid) (Cu@PIL) hybrid which exhibited a moderate selectivity to C_{2+} products (FE_{C2+} = 46.2%, with Cl^- as the anion of Cu@PIL and in 1 M KOH) with a high total current density (> 300 mA cm^{-2}) [29]. The Cu nanoparticles (NPs) were covered with the PIL shell comprising highly dispersed imidazolium-pyridine-imidazolium tridentate sites and a dense electrostatic network. We envisaged the introduction of Pd salts by coordination with both the tridentate sites and the anions at the PIL layer would enable constructing the desired Cu-Pd interfaces for the CO_2RR. The numbers of effective Cu-Pd interfaces could be readily adjusted by the type and dosage of Pd salts, thereby further improving the selectivity of high-value C_{2+} products.

In order to test our hypothesis, a novel Cu@PIL@Pd bimetallic hybrid was facilely obtained by impregnating $PdCl_2$ into the pristine Cu@PIL with Cl^- as the anion. Comprehensive characterizations suggested that the encapsulated palladium existed not only as Pd(II) cations embedded in the PIL layer by coordination with either the tridentate sites or the anions but also in the PdO_2 phase that *in situ* formed by the reaction of $PdCl_2$ with copper species at the surface of Cu NPs. Such a less common Cu_2O-type palladium oxide was surrounded by varied copper species in the PIL layer, thus creating abundant Cu-Pd interfaces. Remarkably, only a small dosage of $PdCl_2$ was required by such a protocol to achieve the Cu-Pd electrocatalyst that outperformed most closely related examples in the generation of C_{2+} products from CO_2RR. Specifically, by employing Cu@PIL@Pd-2.0 with Pd/Cu of 2.0 mol% as the electrocatalyst, a high FE_{C2+} of 68.7% was achieved with a high partial current density of C_{2+} products (178.3 mA cm^{-2}) at the cathodic potential of –1.01 V (with respect to the reversible hydrogen electrode (RHE), the same below). Meanwhile, a high FE_{CH4} of 42.5% and the correspondingly high partial current density of 172.8 mA cm^{-2} were achieved at –1.24 V over the same catalyst, signifying a significant potential-dependent selectivity. The synergetic effects between metal sites and the PIL layer on the CO_2RR process were preliminarily discussed.

2. Materials and methods

2.1. Synthesis of Cu@PIL@Pd-N

Cu@PIL@Pd-N was prepared by impregnating Cu@PIL with $PdCl_2$ salt with different Pd/Cu molar percentages (N). The detailed procedure for the synthesis of Cu@PIL was described in our previous work [29]. Typically, ionic liquid monomer (i.e., 3,3′-(pyridine-2,6-diylbis(methylene))bis(1-vinyl-1H-imidazol-3-ium) chloride) (0.870 g, 2.4 mmol, 1 equiv.), divinylbenzene (0.630 g, 4.8 mmol, 2 equiv.), and azodiisobutyronitrile (0.045 g, 5 wt%) were added to methanol (35 mL) under argon. After stirring at room temperature for one hour, it was heated to 85 °C and refluxed for another one and a half hours. Then, the commercially available Cu NPs (Sigma-Aldrich) with a mean size of 25 nm (0.512 g, 8 mmol, 3.33 equiv.) were dispersed in methanol (20 mL), which was all added to the above mixture. After reacting for 24 h, the resulting suspension was filtrated and washed with methanol (10 mL × 5) to afford Cu@PIL with Cl^- as anions. Subsequently, the obtained Cu@PIL was dispersed in methanol (30 mL) and $PdCl_2$ (0.007 g, 0.04 mmol, 0.016 equiv.) was added at 50 °C. After reacting for 4.5 h, the suspension was filtrated and washed with methanol (20 mL × 5), followed by drying under vacuum at 60 °C overnight, to afford Cu@PIL@Pd-0.5.

The synthesis of Cu@PIL@Pd-N (N = 1.0, 2.0, 4.0) followed the same procedure as that of Cu@PIL@Pd-0.5 but differed in the dosage of $PdCl_2$, wherein $PdCl_2$ (0.014 g, 0.08 mmol, 0.032 equiv.; N = 1.0), $PdCl_2$ (0.028 g, 0.16 mmol, 0.064 equiv.; N = 2.0), and $PdCl_2$ (0.057 g, 0.32 mmol, 0.128 equiv.; N = 4.0) were used, respectively. Besides, the synthesis of PIL@Pd also followed the same procedure as that of Cu@PIL@Pd-0.5, but in the absence of Cu NPs.

2.2. Characterizations

The high-resolution transmission electron microscopy (HR-TEM) images were performed on a JEM-F200 transmission electron microscope with an accelerating voltage of 200 kV (JEOL, Japan). The scanning electron microscopy (SEM) images were collected from a SU8020 scanning electron microscope with an accelerating voltage of 5 kV (Hitachi, Japan). The X-ray diffraction (XRD) patterns were obtained from a Smartlab(9) diffractometer with Cu Kα radiation (40 kV, 150 mA) of wavelength 1.5406 Å (Rigaku, Japan). The X-ray photoelectron spectroscopy (XPS) measurements were performed on an ESCALAB 250Xi X-ray photoelectron spectrometer using Al as the exciting source (ThermoFisher, USA). The gas chromatography (GC) measurements were performed on a 7890-gas chromatography system (Agilent, USA). The ^1H nuclear magnetic resonance (NMR) analyses were conducted with an AVANCE III 600 nuclear magnetic resonance spectrometer (Bruker, Germany). The Raman spectrum was collected from an inVia Qontor confocal Raman microscope (Renishaw, UK).

2.3. Performance evaluation of electrocatalytic CO_2 reduction

All the electrocatalytic tests were performed with a homemade flow cell, which was described in our previous work [29]. The dimensions of the gas and electrolyte solution chambers are 20 mm × 5 mm × 1.5 mm and 20 mm × 5 mm × 3 mm, respectively. The gas diffusion electrodes (GDEs) loaded with Cu@PIL@Pd-N were used as the working electrode. A piece of foamed nickel and a mercuric oxide electrode (in 1 M KOH) was used as the counter and reference electrodes, respectively. The cathodic potentials were converted to a reversible hydrogen electrode (E_R) with iR compensations (85%) after electrolysis:

$$E_R = E_r + 0.098(V) + 0.0592(V) \times pH - iR \times 85\%$$

where E_r is the measured potential, i is the current density, and R is the resistance of electrolyte solution. The selected applied potentials (with respect to the mercuric oxide electrode) were –1.65 V, –1.85 V, –2.05 V, –2.25 V, –2.45 V, and –2.65 V for CO_2RR experiments. An Autolab PGSTAT204N workstation (Metrohm, Switzerland) was employed. An anion exchange membrane (AEM, FAA-3-PK-130, Fumasep) was used to separate the electrolyte solution chambers. KOH solutions (1 M) were used as the catholyte and anolyte solutions. The flow rates of the catholyte and anolyte solutions were set as 2.5 mL min^{-1} and 20 mL min^{-1}, respectively. Pure CO_2 gas (99.999%) was used as the feed gas with a flow rate of 12 mL min^{-1}. In order to accurately measure the flow rate of outlet gas, a soap-film flowmeter was employed.

Gaseous products were analyzed on a GC system. H_2 and CO were analyzed by a TCD equipped with HyaeseepQ and Molsievee 5 Å columns. CH_4, C_2H_6, and C_2H_4 were analyzed by an FID equipped with an HP-PLOT Al_2O_3 column. The faradaic efficiency of gaseous products (FE_G) was calculated:

$$FE_G = \frac{n \times F \times x_G \times R}{i} \times 100\%$$

where n represents the number of electrons transferred, F represents the Faraday constant, x_G represents the fraction of gaseous products, R represents the flow rate of outlet gas. Liquid products were quantified by an NMR spectrometer. 400 μL of electrolyte was added to 200 μL

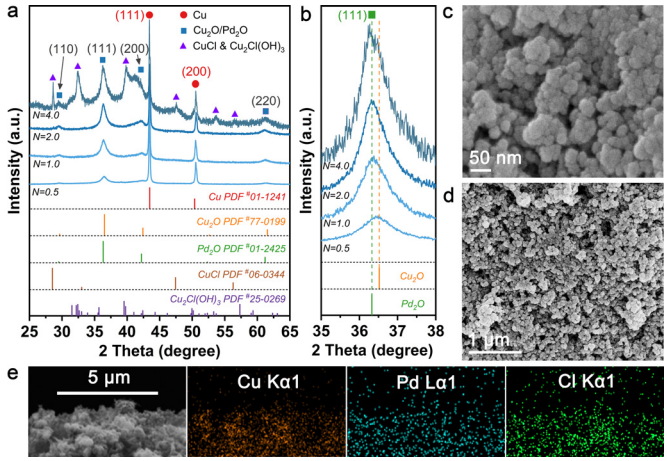

Fig. 1. Crystal structure and morphology characterizations of Cu@PIL@Pd. (a, b) X-ray diffraction (XRD) patterns of Cu@PIL@Pd-N (N = 0.5, 1.0, 2.0, and 4.0). (c, d) Scanning electron microscope (SEM) images of Cu@PIL@Pd-2.0 after being loaded on a gas diffusion electrode (GDE). (e) Cross-sectional SEM and corresponding energy dispersive X-ray (EDX) mapping images of catalyst layers assembled by Cu@PIL@Pd-2.0.

deuterium dioxide. Dimethylsulfoxide and phenol were used as internal standards. The FE of liquid products (FE_L) was calculated:

$$FE_L = \frac{n \times F \times c_L \times V}{Q} \times 100\%$$

where c_L represents the concentration of the product, V represents the volume of electrolyte, Q represents the consumed electricity.

2.4. In situ *Raman test*

In situ Raman test was performed in a custom-made flow cell (Fig. S18), which also consists of three chambers, i.e., one gas chamber and two electrolyte solution chambers, separated by a piece of AEM (FAA-3-PK-130, Fumasep). A graphite rod was used as the counter electrode. The cathodic potential was measured by a mercuric oxide (in 1 M KOH) reference electrode. The flow rates of KOH electrolyte solution (1 M) and CO_2 feed gas (99.999%) were set as 50 mL min^{-1} and 35 mL min^{-1}, respectively. During the test, a 785 nm laser excitation source equipped with a 50 × objective was employed.

3. Results and discussion

3.1. *Characterizations of Cu@PIL@Pd-N*

The crystal structure of Cu@PIL@Pd-N (N = 0.5, 1.0, 2.0, and 4.0) was characterized by the X-ray diffraction (XRD) technique. Herein, the N values denote the Pd/Cu molar percentage for the impregnating $PdCl_2$. As shown in Fig. 1a, the feature patterns of metallic Cu could be clearly identified for all the four materials, while the intensity of peaks at the 2-theta degree of ~36°, ~42°, and ~61° increased with the N values. By carefully identifying the XRD patterns (Figs. 1b and S1), we found an obvious left shift of these peaks compared to those of Cu_2O (PDF#77-0199; i.e., 36.3° *vs.* 36.5°; 42.2° *vs.* 42.4°; 61.2° *vs.* 61.6°), which meant that these diffractive features should be attributed to a less common Cu_2O-type oxide of palladium, namely Pd_2O [30,31]. Furthermore, patterns related to CuCl and $Cu_2Cl(OH)_3$ appeared when N = 4.0, which was probably imposed by the excessive introduction of $PdCl_2$ salt. Scanning electron microscopy (SEM) images (Figs. 1c, d, and S2) showed porous morphologies comprising abundant spheres with a particle size of ~50 nm after these hybrids were loaded on the gas diffusion electrode (GDEs). Cross-sectional SEM and energy dispersive X-ray (EDX) mapping images (Fig. 1e) exhibited the distribution of Cu and Pd elements among the surface layer of the GDE.

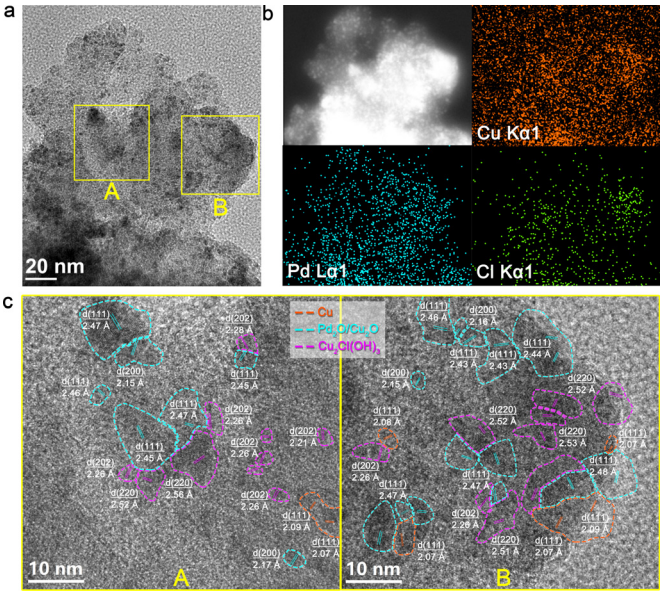

Fig. 2. High-resolution transmission electron microscope (HR-TEM) characterizations of Cu@PIL@Pd-2.0. (a, b) HR-TEM and corresponding EDX mapping images of Cu@PIL@Pd-2.0. (c) Enlarged view of the yellow areas in (a) (left: area A, right: area B; orange, blue, and violet dashed lines circle fragments of Cu metal, Pd_2O (or Cu_2O), and $Cu_2Cl(OH)_3$, respectively).

The high-resolution transmission electron microscopy (HR-TEM) image (Fig. 2a) of Cu@PIL@Pd-2.0 suggested plentiful nanoparticles were highly dispersed in the PIL layer. Besides, the corresponding EDX images (Fig. 2b) demonstrate that Cu and Pd elements dispersed unevenly at the scale of several nanometers. The lattice fringes could be classified into three types by enlarging the marked areas in the HR-TEM image (Fig. 2c): (i) the spacing of the fringes of 2.08 Å, assigning to the (111) inter-planar distance of metallic Cu (highlighted in orange); (ii) the spacing of the fringes of 2.47 Å and 2.14 Å, assigning to the (111) and (200) inter-planar distances of Pd_2O (or Cu_2O, because of the similarities in the crystal structure) (highlighted in light blue); and (iii) the spacing of the fringes of 2.52 Å and 2.27 Å, assigning to the (220) and (202) inter-planar distances of $Cu_2Cl(OH)_3$ (highlighted in light violet). Evidently, nanocrystals of Cu, Pd_2O (or Cu_2O), and $Cu_2Cl(OH)_3$ existed in a highly fragmented manner, which created many phase interfaces, including Cu-Pd_2O (or Cu_2O), $Cu_2Cl(OH)_3$-Pd_2O (or Cu_2O), Pd_2O (or Cu_2O)-Pd_2O (or Cu_2O), Cu-$Cu_2Cl(OH)_3$, and $Cu_2Cl(OH)_3$-$Cu_2Cl(OH)_3$ interfaces. Despite the difficulties in accurately distinguishing Pd_2O from Cu_2O phases, we supposed many Cu-Pd phase interfaces should be created. Such a viewpoint can be supported by both experiments and related literature: (i) the diffracted intensity for Pd_2O is quite strong in the XRD characterizations (Fig. 1a), corresponding to the presence of numerous crystal phases of Pd_2O; (ii) the formation of stable Pd(I) oxide was documented only on or near (with) excess metals, such as metallic Cu, Hg, Mn, and Pd [31,32].

The X-ray photoelectron spectroscopy (XPS) was conducted to reveal the oxidation state of different elements at the surface of Cu@PIL@Pd-N (Figs. 3 and S3–S6). Cu LMM Auger spectra (Fig. 3a) suggested five peaks at the kinetic energy (KE) of 918.7 eV, 916.8 eV, 916.3 eV, 915.4 eV, and ~914 eV, assigning to metallic Cu [33], Cu hydroxides [34], Cu_2O [35], Cu chlorides [36, 37], and Cu chelated by organic ligands [38]. Besides, the intensity of copper hydroxides and copper chlorides in Cu@PIL@Pd-N was enhanced, while that of metallic Cu, Cu_2O, and chelated Cu was weakened, with the increase of the N values. It implied that the added $PdCl_2$ might react with Cu or Cu_2O to form Pd_2O "coating" the surface of Cu NPs.

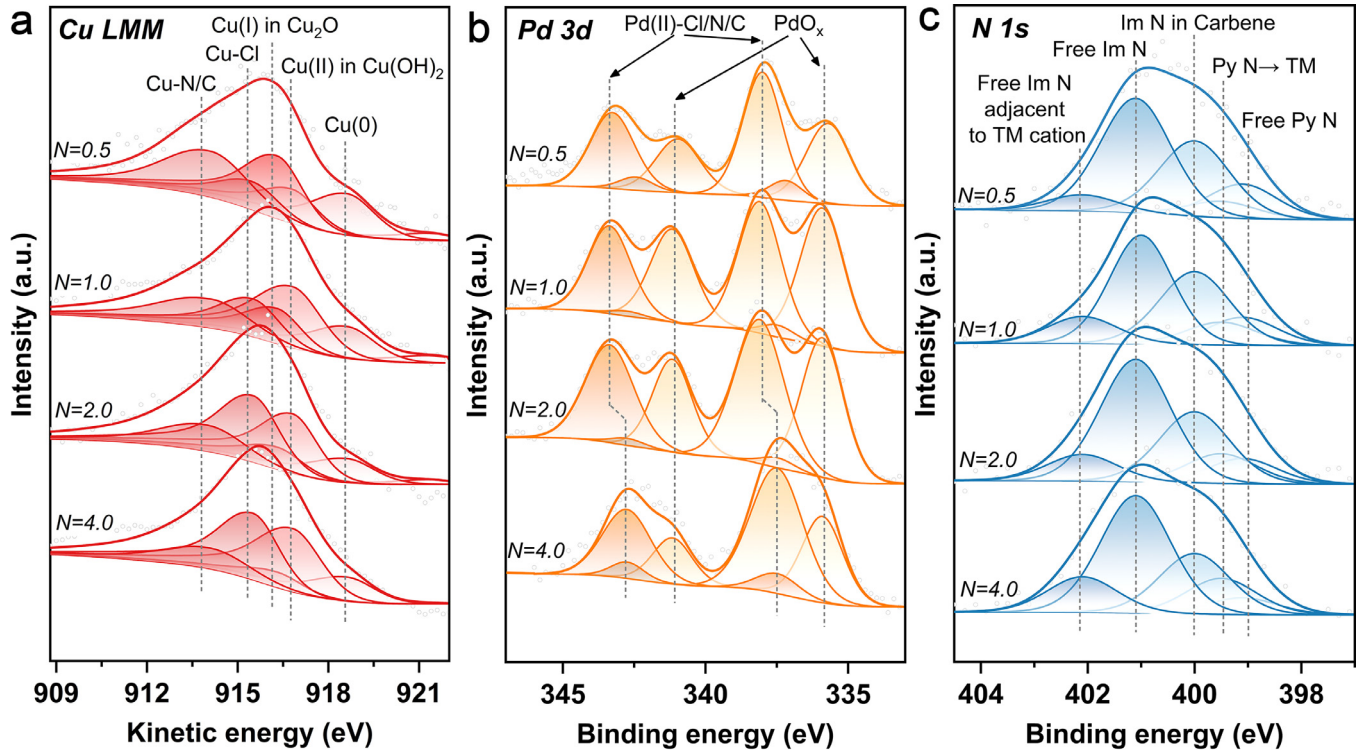

Fig. 3. Auger and X-ray photoelectron spectroscopy (XPS) spectra of Cu@PIL@Pd. (a-c) Cu LMM Auger spectra, high-resolution Pd 3d XPS spectra, and high-resolution N 1s XPS spectra of Cu@PIL@Pd-N. (Abbreviations: Im denotes imidazolium, Py denotes pyridinic, TM denotes transition metal.)

The high-resolution XPS spectra in the Pd 3d region displayed two pairs of spectral features in Fig. 3b. Two broad peaks at the relatively higher binding energies (BEs) of 338.0 eV and 343.3 eV were assigned to Pd(II) species in Cu@PIL@Pd-N (N = 0.5, 1.0, 2.0) [39]. Herein, it is difficult to exactly identify the precise structure of these species since the BEs of Pd(II) chlorides and Pd(II) complexes cover a wide range of 337.4 to 338.5 eV (Table S3). By contrast, an evident shift to lower BE was observed for Cu@PIL@Pd-4.0 impregnated with more $PdCl_2$ salt. It suggested Pd(II) chlorides should possess lower BE therein. Besides, the Pd 3d XPS spectra also contained two intense peaks at the relatively lower BE of 335.8 and 341.1 eV. Notably, the former at 335.9 eV was located between the feature peaks of PdO (336.5 eV) and metallic Pd (335.3 eV) [40], which thus should be attributed to PdO_x ($x < 1$), namely Pd_2O.

In the N 1s XPS spectra (Fig. 3c), the presence of free pyridinic nitrogen at 399.1 eV and free imidazolium nitrogen at 401.2 eV [41,42] decorated at the PIL layer was observed. In addition, the corresponding transition metal-chelated species feature at 399.5 eV and 400.0 eV [43], signifying the coordination interaction of the PIL layer with Cu and Pd elements, respectively. It also contained one peak in a high BE region (402.1 eV). The less free charges of such imidazolium nitrogen (Im $N^{\delta+}$) could be attributed to the electrostatic interaction with Cl anions embedded in the PIL layer. We supposed such electrostatic interactions still exist between Pd cations and Cl anions and these highly dispersed electrostatic interaction networks (Im $N^{\delta+}$…$Cl^{\delta-}$…$Pd^{\delta+}$) by introducing $PdCl_2$ to the surface of Cu@PIL may further improve the conductivity of the PIL layer. The presence of a joint chloride site surrounded by various cations was confirmed by the apparent peaks at ~199.6 eV in the Cl 2p XPS spectra (Figs. S3d–S6d).

Based on the above characterization and discussion, the potential reaction process during the impregnation, wherein the metallic Cu or Cu oxide (mainly Cu_2O) functioned as the reductant, was summarized in Table 1. At the metallic surface of Cu NPs, Cu reacted with the upcoming $PdCl_2$ to deliver Pd and $CuCl_2$, wherein the nano-sized Pd quickly turned into Pd_2O upon exposure to air. Alternatively, Cu_2O at the oxidized surface of Cu NPs could react directly with $PdCl_2$ to provide Pd_2O and $CuCl_2$. Meanwhile, the formation of $Cu_2Cl(OH)_3$ was most likely attributed to the hydrolysis of $CuCl_2$ with the moisture in the atmosphere. The coincidentally released HCl is prone to undergo a double replacement reaction with Cu_2O to give CuCl. Moreover, CuCl may also be formed *via* the comproportionation reaction between Cu and $CuCl_2$. In principle, such redox reactions between copper and palladium could be classified as the galvanic replacement reaction (GRR) [44]. This strategy was demonstrated to facilitate the formation of the bimetallic interface rather than alloy. As a proof of concept, Cu-Ag bimetallic catalysts were synthesized thereby for high-performance CO_2RR [44].

Table 1
Reaction equation of $PdCl_2$ salt with metallic Cu or Cu oxide during the impregnation.

Classification	Reaction equation
The formation of Pd_2O on metallic Cu surface	$Cu + PdCl_2 \rightarrow CuCl_2 + Pd$ $4Pd + O_2 \rightarrow 2Pd_2O$
The formation of Pd_2O on Cu oxide surface	$Cu_2O + PdCl_2 \rightarrow CuCl_2 + Pd_2O$
The formation of $Cu_2Cl(OH)_3$ and CuCl	$2CuCl_2 + 3H_2O \rightarrow Cu_2Cl(OH)_3 + 3HCl$ $2HCl + Cu_2O \rightarrow 2CuCl + H_2O$ $Cu + CuCl_2 \rightarrow 2CuCl$

3.2. Electrocatalytic CO_2RR on Cu@PIL@Pd-N

In order to accelerate the mass transfer of CO_2, a flow cell equipped with a gas chamber was employed to carry out the CO_2RR experiments. The catalytic performance of Cu@PIL@Pd-N at the selected applied cathodic potentials was examined and the results were displayed in Fig. 4. Taking Cu@PIL@Pd-0.5 as an example, the total current density (j_{total}) increased rapidly from 59.6 to 412.6 mA cm^{-2} with the cathodic poten-

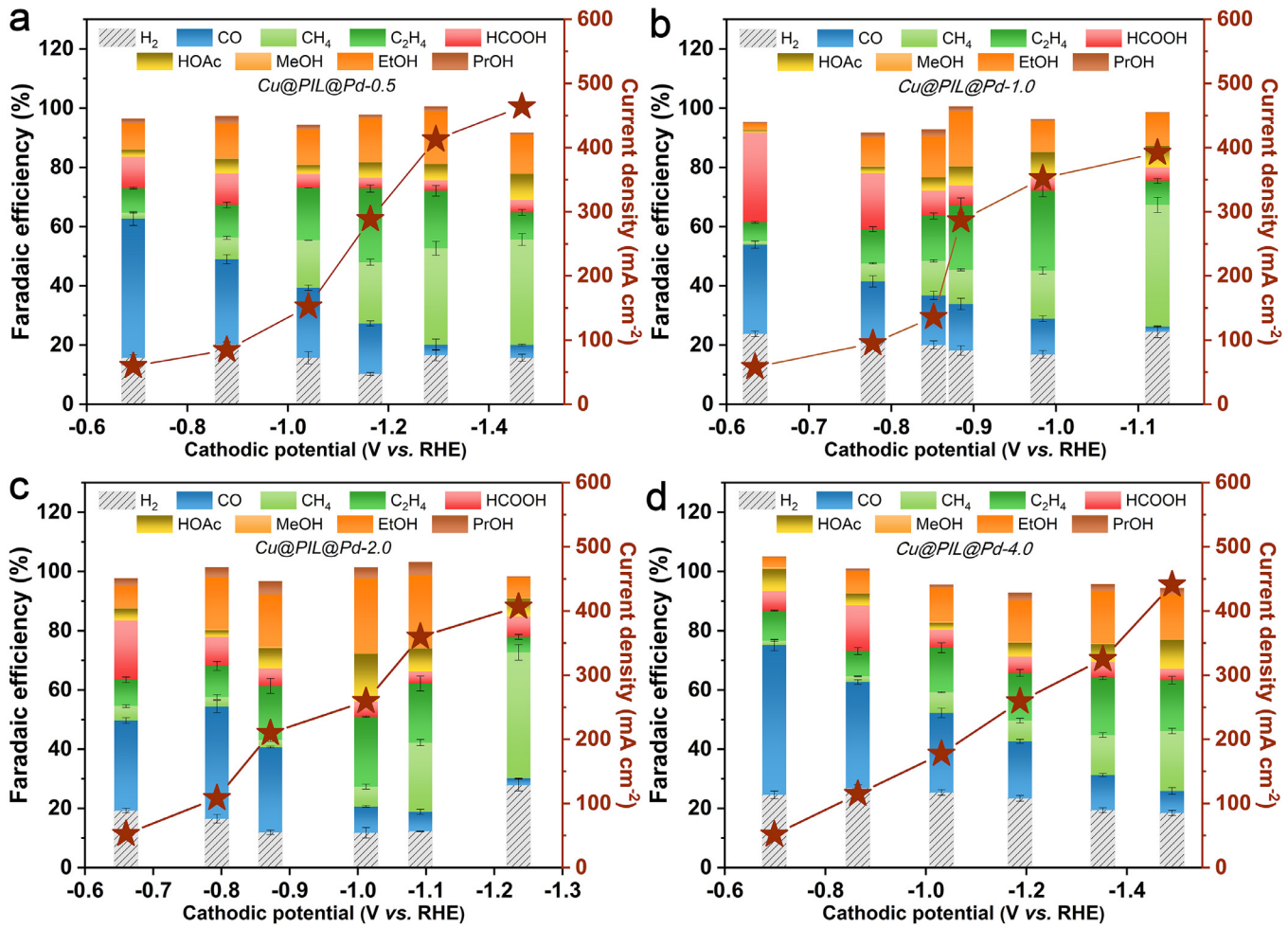

Fig. 4. Electrocatalytic CO_2RR performance of Cu@PIL@Pd. (a–d) Faradaic efficiency and current density of Cu@PIL@Pd-N during CO_2RR at different cathodic potentials. Note: all the CO_2RR experiments were conducted with the same applied cathodic potentials (with respect to the mercuric oxide electrode). The recorded compensated cathodic potentials (with respect to the reversible hydrogen electrode) were calculated according to the equation in Section 2.3.

tial ($E_{cathodic}$) negatively shifting from −0.69 to −1.29 V, then slowly reached the potential value by further increasing the $E_{cathodic}$. The highest j_{total} of 464.1 mA cm^{-2} was obtained at −1.47 V. In comparison, no greater j_{total} was obtained for Cu@PIL@Pd-N (N = 1.0, 2.0, 4.0) impregnated with more $PdCl_2$. The corresponding j_{total} obtained at the same negative applied potential of –2.65 V (with respect to the mercuric oxide electrode) were 392.01 mA cm^{-2} (N = 1.0), 406.73 mA cm^{-2} (N = 2.0), and 441.2 mA cm^{-2} (N = 4.0), respectively.

The product distribution was similar for Cu@PIL@Pd-0.5, Cu@PIL@Pd-1.0, and Cu@PIL@Pd-2.0. When the applied $E_{cathodic}$ shifted negatively forward, the FE_{CO} gradually decreased, coincidently with the increase of the FE_{CH4}. In contrast, the FE_{C2+} reached the maximum value at a moderate $E_{cathodic}$. Representatively, the highest FE_{C2+} on Cu@PIL@Pd-2.0 was obtained at –1.01 V. With more negative $E_{cathodic}$ (i.e., –1.09 V to –1.24 V), the FE_{C2+} rapidly decreased accompanied by the increase of the FE_{CH4} (Fig. S7). These results demonstrated that there was a significant potential-dependent competition between the hydrogenation of CO* and the C–C coupling reaction after the formation of CO over Cu@PIL@Pd-N (N = 0.5, 1.0, 2.0). However, both the FE_{CH4} and FE_{C2+} increased on Cu@PIL@Pd-4.0 with negatively shifting the $E_{cathodic}$. It provided poor values of 20.3% and 44.4%, respectively, even at a high overpotential ($E_{cathodic}$ = −1.49 V). The greatest FE_{CO} value within the same range of the $E_{cathodic}$ on Cu@PIL@Pd-4.0 compared to the other Cu@PIL@Pd-N (N = 0.5, 1.0, 2.0) hybrids (Fig. S8) indicated that too much $PdCl_2$ was not conducive to generating multi-electron reduction intermediates (i.e., CHO* or *COOC*) from CO, despite the presence of significant copper-based chlorides and hydroxides therein (Fig. 1a) that in principle should facilitate both the hydrogenation of CO* and the C–C coupling reaction [17].

The highest FE_{C2+} of 68.7% was obtained on Cu@PIL@Pd-2.0 at the $E_{cathodic}$ of –1.01 V with a high partial current density of C_{2+} products (j_{C2+} = 178.3 mA cm^{-2}), which was the best record compared with the reported values for generating C_{2+} products on Cu-Pd based electrocatalysts (Table S5). Note that a higher j_{C2+} of 204.6 mA cm^{-2} was achieved at the $E_{cathodic}$ of –1.09 V, but with a reduced C_{2+} selectivity (FE_{C2+} = 56.8%). In comparison, the highest FE_{C2+} on the other Cu@PIL@Pd-N hybrids are relatively worse, recording as 46.2% (N = 0.5), 48.5% (N = 1.0), and 45.3% (N = 4.0), respectively. On the other hand, we found that the occupation of C_2H_4 composite in the highest FE_{C2+} differed slightly on Cu@PIL@Pd-0.5 (FE_{C2H4}: 25.0%), Cu@PIL@Pd-1.0 (FE_{C2H4}: 27.1%), and Cu@PIL@Pd-2.0 (FE_{C2H4}: 23.6%) (Fig. S9). The best selectivity toward C_{2+} products obtained on Cu@PIL@Pd-2.0 was mainly attributed to the highest FE_{EtOH} value of 25.3%, suggesting the presence of numerous Cu-Pd interfaces in this case [24,25]. Besides, the best FE_{CH4} of 42.5% was also achieved on Cu@PIL@Pd-2.0 at –1.24 V, corresponding to a high j_{CH4} of 172.8 mA cm^{-2}. Notably, such a high j_{CH4} value was superior to not only that on Pd-based electrocatalyst but also those on many other advanced electrocatalysts (Table S6). The outstanding performance towards both

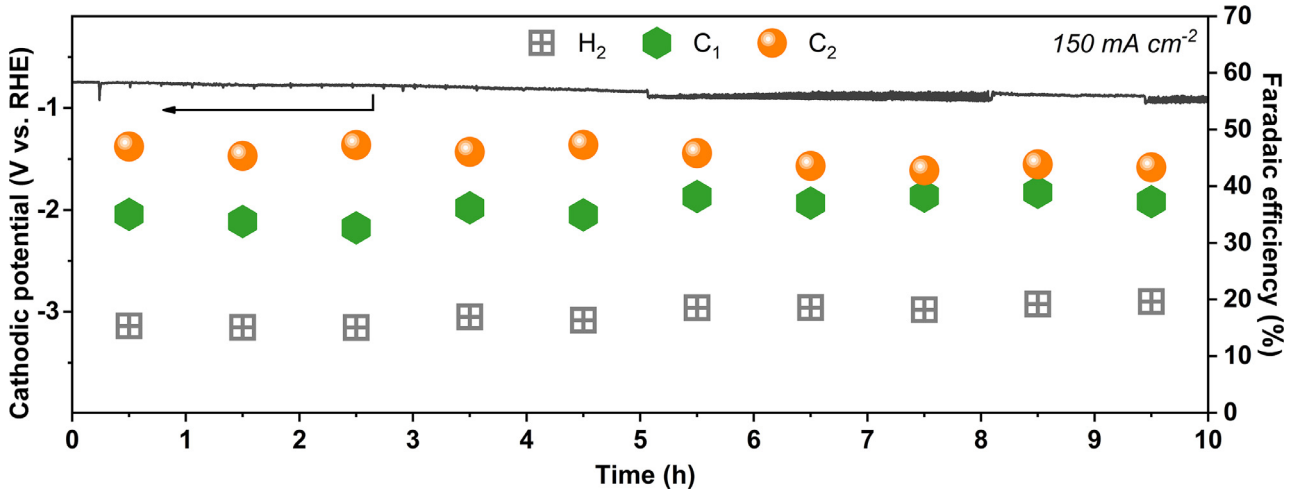

Fig. 5. Long-term stability test of Cu@PIL@Pd-2.0 in KOH solution (1 M) at 150 mA cm^{-2} for 10 h.

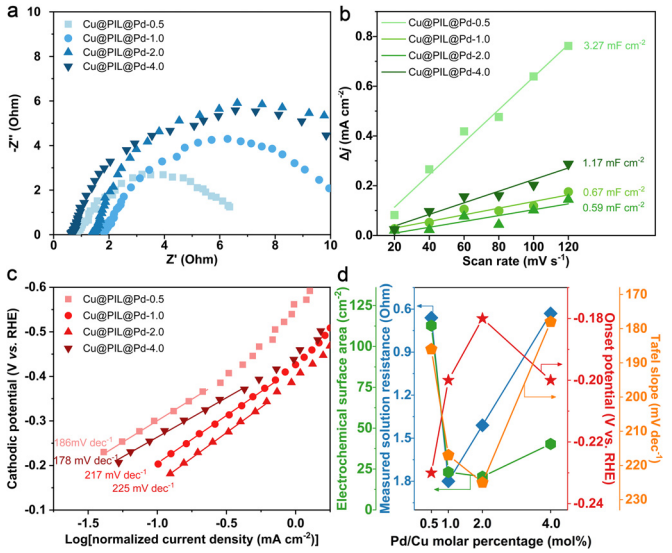

Fig. 6. Electrochemical studies of Cu@PIL@Pd. (a) Electrochemical impedance spectroscopy (EIS) spectra of Cu@PIL@Pd-N at –0.3 V (*vs.* RHE). (b) Current density differences (Δ*j*) of cyclic voltammetry (CV) curves at 0.45 V (*vs.* RHE) for Cu@PIL@Pd-N plotted against scan rate. (c) Tafel plots for Cu@PIL@Pd-N. (d) The measured solution resistances, electrochemical surface areas, onset potentials, and Tafel slopes of Cu@PIL@Pd-N.

the C_{2+} products and CH_4 on Cu@PIL@Pd-2.0 suggested that the formation and subsequent conversion of CO* was very rapid.

The long-term electrolysis (10 h) over Cu@PIL@Pd-2.0 was performed at 150 mA cm^{-2} in 1 M KOH to test the catalytic durability. As shown in Fig. 5, a slight fluctuation of the $E_{cathodic}$ in the range from –0.76 to –0.83 V (with *iR* compensation) could be observed within the first 5 h. Subsequently, the $E_{cathodic}$ further negatively shifted to around –0.90 V with a more intensive fluctuation, which was highly likely imposed by not only the flooding and carbonation of the microporous layer of GDE but also the continuous acidification of the electrolyte solution. On the other hand, the variation of FE_{C2+} was not significant during this period. After 10 h electrolysis, the selectivity towards C_{2+} products decreased by only 3.7% (from 47.0% to 43.3%), demonstrating good stability of this PIL-based Cu-Pd bimetallic catalyst.

The electrochemical behaviors of Cu@PIL@Pd-N were next investigated (Figs. 6a–c, and S10, S11), and the measured solution resistance (R_s), the electrochemical surface area (ECSA), the onset potential, and the Tafel slope were summarized in Fig. 6d and Tables S1, S2. It's worthy to note that the PIL layer could be considered as a thin layer of "solid" electrolyte surrounding the active sites for the CO_2RR. Therefore, the measured R_s was imposed by two parts: the resistance of electrolyte solution (i.e., 1 M KOH) and the resistance of the PIL layer. In this regard, the variation of R_s accounted for the different conductivity of the PIL layer to a certain extent, since the structure and the composition of the flow cell remained unchanged. Evidently, Cu@PIL@Pd-0.5 possessed the lowest R_s resistance of 0.66 ohm and the highest ECSA of 112.76 cm^2, corresponding to the lowest barrier for the charge transfer and the presence of abundant active sites. However, the reaction rate on Cu@PIL@Pd-0.5 was much lower than that on Cu@PIL@Pd-1.0 and Cu@PIL@Pd-2.0 (Fig. S12), which possessed higher R_s and lower ECSA, at the same $E_{cathodic}$, suggesting the charge transfer and the number of the general active site were not the limiting factors for the multi-electron reduction of CO_2.

The Tafel plot analysis indicated Cu@PIL@Pd-2.0 had the most positive onset potential (–0.18 V) and the largest normalized initial current density, which meant the fastest kinetics in CO generation. Besides, the moderate Tafel slope of 225 mV dec^{-1} on Cu@PIL@Pd-2.0 was attributed to the slow diffusion of CO_2. These results demonstrated that CO could be readily produced (mainly on palladium composition [21–23]) but difficult to desorb, thereby enriching the local CO for subsequent reactions. Meanwhile, the spillover of CO from palladium site to copper site might competitively proceed [24,28], thereby further accelerating the C–C coupling reaction and promoting the selectivity toward the C_{2+} products.

3.3. Mechanistic studies

In order to study the mechanism, this bimetallic catalyst was "divided" into two parts: the palladium dispersed in PIL (denoted as PIL@Pd) and the PIL coated Cu NPs (namely, Cu@PIL). PIL@Pd was independently synthesized by impregnating $PdCl_2$ to the pristine PIL without Cu NPs inside. The XRD test of PIL@Pd demonstrated that the crystal composition was mainly the $PdCl_2$ phase (Fig. 7a). Besides, the absence of the Pd_2O phase confirmed it only formed with Cu NPs in the Cu@PIL@Pd hybrids. Moreover, the HR-TEM images of PIL@Pd (Figs. 7b, c, and S13) suggested the $PdCl_2$ NPs were highly dispersed in the PIL layer, while the SEM image (Fig. S14) displayed a similar morphology to Cu@PIL@Pd (Figs. 1c and S2). A comprehensive XPS analysis showed PIL@Pd was composed of $PdCl_2$ and the chelated Pd(II) species (Fig. S15). We also noticed that the metallic Pd was partially formed in PIL@Pd (Fig. 7a), which might be attributed to the reduction of Pd(II) with methanol during impregnating $PdCl_2$ into PIL [45].

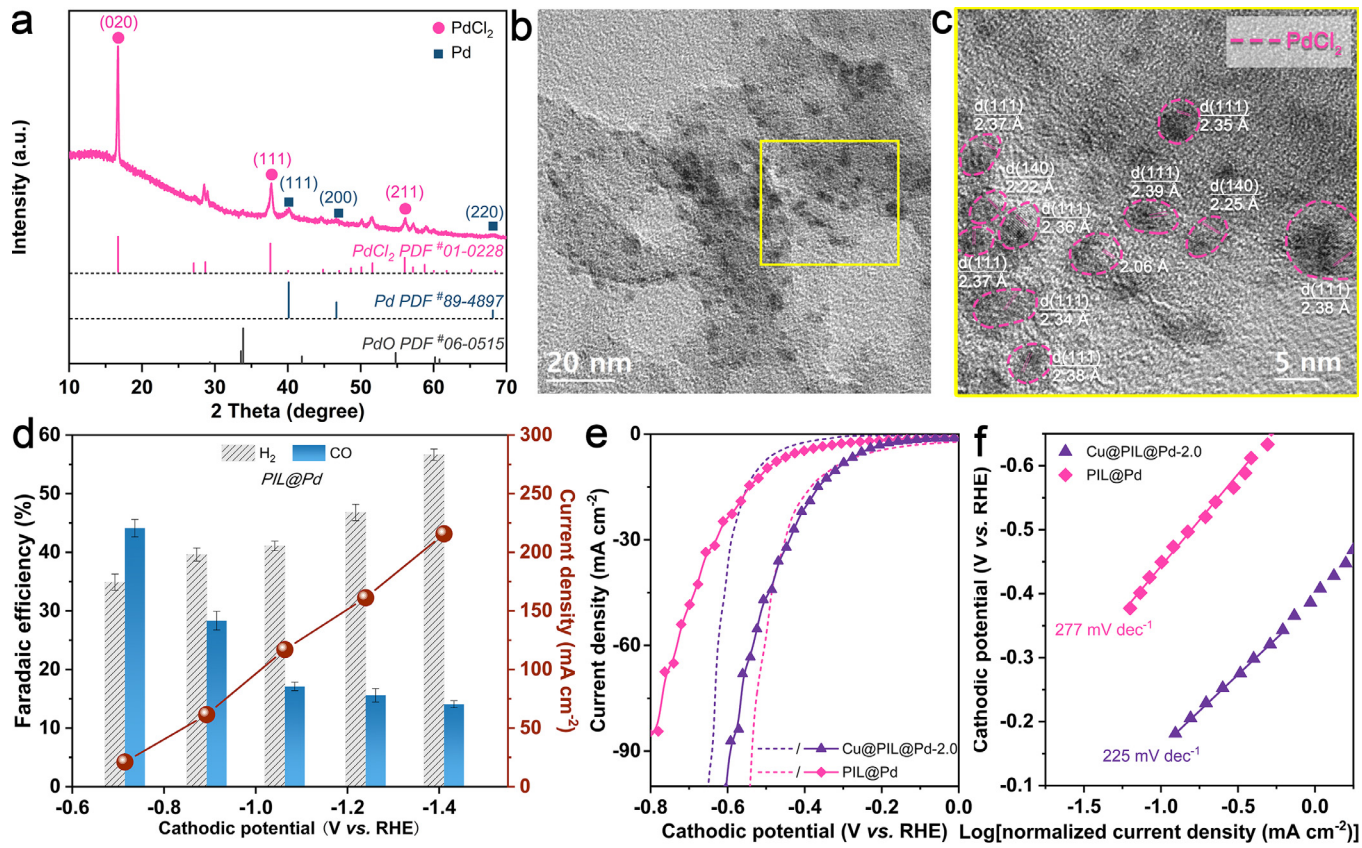

Fig. 7. Characterizations and electrocatalytic CO_2RR performance of PIL@Pd. (a) XRD patterns of PIL@Pd. (b, c) HR-TEM images of PIL@Pd. (d) Faradaic efficiencies (FEs) of H_2 and CO during CO_2RR on PIL@Pd at different cathodic potentials. (e) Linear sweep voltammetry (LSV) plots of PIL@Pd and Cu@PIL@Pd-2.0 (dashed line: with N_2 supply, solid line with symbol: with CO_2 supply). (f) Tafel plots of PIL@Pd and Cu@PIL@Pd-2.0.

The CO_2RR performance of PIL@Pd only exhibited selectivity towards CO (Fig. 7d), corresponding to the documented features of Pd-based electrocatalysts [21–23]. Furthermore, the FE_{CO} decreased with the increase of the FE_{H2}, which was also observed on Pd(II) cations coordinated by tridentate Schiff base ligands [46]. It suggested Pd(II) cations embedded in the PIL layer by coordinating with either the tridentate sites or the anions, besides the PdO_2 phase, might account for the production of CO during the CO_2RR. The LSV plots in Fig. 7e showed the current density with the N_2 supply was less than that with the CO_2 supply at the same $E_{cathodic}$ on Cu@PIL@Pd-2.0. However, the much larger opposite difference in the current density with both supplies for PIL@Pd, corresponding to its high selectivity towards H_2, as demonstrated in Fig. 7d.

By contrast, Cu@PIL possessed good CO_2RR performance for C_{2+} production [29]. The highest FE_{C2+} was 46.2% on Cu@PIL with Cl^- as the anion in 1 M KOH electrolyte solution (Table S7), demonstrating the C–C coupling reaction mainly occurred on the Cu sites. [29] Meanwhile, the FE_{H2} was kept at a low level (< 20%) [29], suggesting the presence of copper species was conductive to inhibit the hydrogen evolution reaction on PIL-based materials. However, compared with the CO_2RR performance on Cu@PIL@Pd-2.0 (68.7%) under identical conditions, such a FE_{C2+} was much lower. It signified the introduction of palladium could effectively promote the C–C coupling reaction on the adjoint Cu atoms. Furthermore, the onset potential, the initial current density, and the Tafel slope of PIL@Pd were much less than those of Cu@PIL@Pd (Fig. 7f), demonstrating slower formation kinetics of CO without copper. We supposed the presence of Cu species might promote the generation of CO on Pd sites since highly mixed Cu-Pd materials were reported to show high FE_{CO} [24,47].

The *in situ* Raman (Figs. 8 and S19) test was employed to study the oxidation state of Cu and Pd species on Cu@PIL@Pd-2.0 during the CO_2RR. At the open circuit potential (OCP) and the $E_{cathodic}$ of 0.53 V (Figs. 8a and S19a), besides the spectral features related to Cu_2O (147 cm^{-1}, 528 cm^{-1}, and 620 cm^{-1}) [48]. two weak peaks at 223 cm^{-1} and 646 cm^{-1} assigned to palladium oxide were observed [49]. These features decayed rapidly once the $E_{cathodic}$ negatively shifted over 0.33 V, suggesting all the copper and palladium oxides were reduced to Cu(0) and Pd(0) species during the CO_2RR. Besides, the peak at 357 cm^{-1} was assigned to the CO* adsorbed on Cu and Pd sites (Cu-CO and Pd-CO) [48,49], which disappeared once the $E_{cathodic}$ was removed together with a rapid re-oxidation of copper and palladium (Fig. S19). Furthermore, the comprehensive characterizations of the used catalyst suggested that the crystal structure and the morphology basically were retained during the CO_2RR (Figs. S20, S21). However, there formed more copper oxides (i.e., Cu_2O and CuO) with the disappearance of copper chlorides, while the types and the distribution of palladium species were identical to those in the fresh samples (Fig. S22). It demonstrated that the valence variation of copper (Cu(I)/(II) oxides/chlorides → Cu(0) → Cu(I)/(II) oxides) and palladium (Pd(I) oxides → Pd(0) → Pd(I) oxides) species at the surface of Cu@PIL@Pd-2.0 during an electrolysis cycle. These results indicated that the metallic Cu/Pd species, rather than the Cu/Pd oxides, persisted in the CO_2RR catalytic activity. Meanwhile, only one peak at 2050 to 2071 cm^{-1} existed within the wavenumber range from 1700 to 2400 cm^{-1} (Fig. 8c), which corresponded to the stretching vibration mode of CO* [18]. Such a Raman shift was a little lower than that on Cu@PIL (2089 to 2095 cm^{-1}) [29]. We thus attributed this peak to the stretching vibration mode of CO* on Pd (ν(Pd-CO)). The assignments of other Raman peaks are summarized in Table S4.

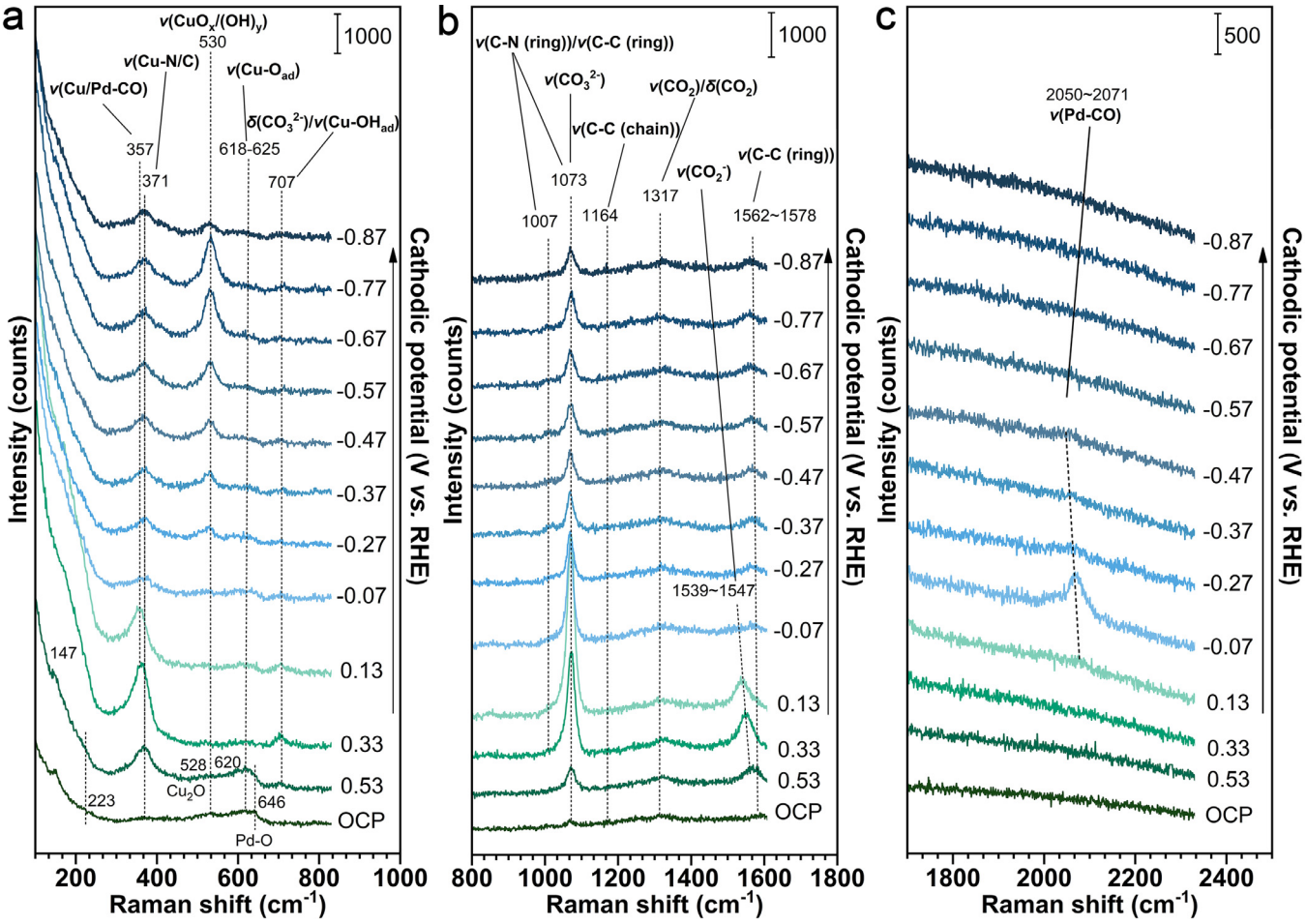

Fig. 8. *In situ* Raman study of Cu@PIL@Pd-2.0. *In situ* Raman spectra on GDE loaded with Cu@PIL@Pd-2.0 at the different cathodic potential in the Raman shift ranges of (a) 100 to 800 cm^{-1}, (b) 800 to 1700 cm^{-1}, and (c) 1700 to 2400 cm^{-1}.

Collectively, the synergy effect caused by Cu and Pd could be summarized as (i) Cu can promote the generation of CO on the adjoint Pd sites, including the *in -situ* formed Pd_2O and the immobilized Pd(II) cations; and (ii) the abundant Cu-Pd interfaces are conducive to the spillover of CO* from Pd sites to the adjoint Cu sites, thereby promoting the C–C coupling reaction. In addition, in comparison to the traditional Cu-Pd bimetallic catalyst, the distinct feature obtained by Cu@PIL@Pd could be attributed to the presence of the PIL layer. The positive influence of the PIL layer on the CO_2RR performance is summarized as: (i) the PIL layer was an ideal medium for high dispersion of different active sites benefitting from the plenty of chelate and the electrostatic sites; (ii) the diffusion of the generated CO was hindered by the PIL layer [50], enabling the local enrichment of CO; and (iii) the dense electrostatic network of the PIL layer, especially when abundant metal cations were introduced, could enhance the conductivity of the entire materials, resulting in the improvement of reaction rate of CO_2RR.

4. Conclusion

In summary, a novel Cu-Pd bimetallic electrocatalyst (Cu@PIL@Pd) was readily obtained by impregnating $PdCl_2$ salt into the Cu@PIL hybrids. As expected, the Pd(II) cations were immobilized in the PIL layer *via* the coordination with the decorated imidazolium-pyridine-imidazolium tridentate sites and the highly dispersed anions to deliver an enhanced electrostatic network, which was conducive to the charge transfer among the PIL layers. Besides, a less-common Cu_2O-type palladium oxide (Pd_2O) was formed from the reaction of $PdCl_2$ with metallic Cu and Cu_2O at the surface of Cu NPs, enabling creating plentiful Cu-Pd interfaces for promoting the C–C coupling reaction. With such a protocol, a small dosage of palladium composite was enough to deliver efficient Cu-Pd-based electrocatalysts for CO_2RR. Mechanistic studies revealed both copper and palladium oxides were reduced to metallic states Cu(0) and Pd(0), respectively at the cathodic potential where CO_2RR begins. The presence of the adjoint copper phase and the highly dispersed electrostatic layer promoted the generation of CO on the palladium components (both the PdO_2 phase and the Pd(II) site). Besides, the local CO* was enriched by the significant diffusion resistance of CO in the PIL layer. The spillover of *CO from Pd sites to the adjoint Cu sites, accompanied by the increased local concentration of *CO around Cu sites, accounted for the observed good CO_2RR catalytic performance, especially the high C_{2+} product selectivity. These findings provided a platform for the novel design concept of CO_2RR catalysts for achieving both efficiency and selectivity toward high-value multi-electron (more than 2 electrons) reduction products.

Declaration of competing interest

The authors declare that they have no conflicts of interest in this work.

Acknowledgments

We also sincerely appreciate Prof. Suo-Jiang Zhang at IPE for his kind suggestions on the topic. Financial support from Key Research Pro-

gram of Frontier Sciences, CAS (ZDBS-LY-JSC022), Excellent Young Scientists Fund (22022815), National Natural Science Foundation of China (U1704251 and 21776291), and Zhengzhou High Level Talent Certificate (20180200052) is gratefully acknowledged.

References

[1] N.W. Kinzel, C. Werle, W. Leitner, Transition metal complexes as catalysts for the electroconversion of CO_2 : an organometallic perspective, Angew. Chem. Int. Ed. 60 (2021) 11628–11686.

[2] Y. Zou, S. Wang, An investigation of active sites for electrochemical CO_2 reduction reactions: from *in situ* characterization to rational design, Adv. Sci. 8 (2021) 2003579.

[3] M.B. Ross, P. De.Luna, Y. Li, et al., Designing materials for electrochemical carbon dioxide recycling, Nat. Catal. 2 (2019) 648–658.

[4] D. Chen, L. Xu, H. Liu, et al., Rough-surfaced bimetallic copper–palladium alloy multicubes as highly bifunctional electrocatalysts for formic acid oxidation and oxygen reduction, Green Energy Environ. 4 (2019) 254–263.

[5] Y. Quan, J. Zhu, G. Zheng, Electrocatalytic reactions for converting CO_2 to value-added products, Small Sci. (2021) 2100043.

[6] S.J. Davis, K. Caldeira, H.D. Matthews, Future CO_2 emissions and climate change from existing energy infrastructure, Science 329 (2010) 1330–1333.

[7] Z. Li, R. Wu, L. Zhao, et al., Metal-support interactions in designing noble metal-based catalysts for electrochemical CO_2 reduction: recent advances and future perspectives, Nano Res. 14 (2021) 3795–3809.

[8] R. Shi, J. Guo, X. Zhang, et al., Efficient wettability-controlled electroreduction of CO_2 to CO at Au/C interfaces, Nat. Commun. 11 (2020) 3028.

[9] D.M. Weekes, D.A. Salvatore, A. Reyes, et al., Electrolytic CO_2 reduction in a flow cell, Acc. Chem. Res. 51 (2018) 910–918.

[10] Y. Kim, S. Park, S.J. Shin, et al., Time-resolved observation of C–C coupling intermediates on Cu electrodes for selective electrochemical CO_2 reduction, Energ. Environ. Sci. 13 (2020) 4301–4311.

[11] M.R. Singh, Y. Kwon, Y. Lum, et al., Hydrolysis of electrolyte cations enhances the electrochemical reduction of CO_2 over Ag and Cu, J. Am. Chem. Soc. 138 (2016) 13006–13012.

[12] D. Raciti, C. Wang, Recent advances in CO_2 reduction electrocatalysis on copper, ACS Energy Lett., 3 (2018) 1545–1556.

[13] A.A. Peterson, J.K. Nørskov, Activity descriptors for CO_2 electroreduction to methane on transition-metal catalysts, J. Phys. Chem. Lett. 3 (2012) 251–258.

[14] K.P. Kuhl, T. Hatsukade, E.R. Cave, et al., Electrocatalytic conversion of carbon dioxide to methane and methanol on transition metal surfaces, J. Am. Chem. Soc. 136 (2014) 14107–14113.

[15] J. Wang, T. Cheng, A.Q. Fenwick, et al., Selective CO_2 electrochemical reduction enabled by a tricomponent copolymer modifier on a copper surface, J. Am. Chem. Soc. 143 (2021) 2857–2865.

[16] H.S. Jeon, S. Kunze, F. Scholten, et al., Prism-shaped cu nanocatalysts for electrochemical CO_2 reduction to ethylene, ACS Catal. 8 (2017) 531–535.

[17] K. Ye, A. Cao, J. Shao, et al., Synergy effects on Sn-Cu alloy catalyst for efficient CO_2 electroreduction to formate with high mass activity, Sci. Bull. 65 (2020) 711–719.

[18] Z.Z. Niu, F.Y. Gao, X.L. Zhang, et al., Hierarchical copper with inherent hydrophobicity mitigates electrode flooding for high-rate CO_2 electroreduction to multicarbon products, J. Am. Chem. Soc. 143 (2021) 8011–8021.

[19] J. Gao, H. Zhang, X. Guo, et al., Selective C-C coupling in carbon dioxide electroreduction via efficient spillover of intermediates as supported by operando Raman spectroscopy, J. Am. Chem. Soc. 141 (2019) 18704–18714.

[20] R.M. Aran-Ais, D. Gao, B.Roldan Cuenya, Structure- and electrolyte-sensitivity in CO_2 electroreduction, Acc. Chem. Res., 51 (2018) 2906–2917.

[21] D. Gao, H. Zhou, F. Cai, et al., Pd-containing nanostructures for electrochemical CO_2 reduction reaction, ACS Catal. 8 (2018) 1510–1519.

[22] Y. Zhou, N. Han, Y. Li, Recent progress on Pd-based nanomaterials for electrochemical CO_2 reduction, Acta Phys. Chim. Sin. 0 (2020) 2001040–2001041.

[23] D. Gao, H. Zhou, J. Wang, et al., Size-dependent electrocatalytic reduction of CO_2 over Pd nanoparticles, J. Am. Chem. Soc. 137 (2015) 4288–4291.

[24] S. Ma, M. Sadakiyo, M. Heima, et al., Electroreduction of carbon dioxide to hydrocarbons using bimetallic Cu-Pd catalysts with different mixing patterns, J. Am. Chem. Soc. 139 (2017) 47–50.

[25] F.Y. Zhang, T. Sheng, N. Tian, et al., Cu overlayers on tetrahexahedral Pd nanocrystals with high-index facets for CO_2 electroreduction to alcohols, Chem. Commun. 53 (2017) 8085–8088.

[26] R. Feng, Q. Zhu, M. Chu, et al., Electrodeposited Cu–Pd bimetallic catalysts for the selective electroreduction of CO_2 to ethylene, Green Chem. 22 (2020) 7560–7565.

[27] L. Zhu, Y. Lin, K. Liu, et al., Tuning the intermediate reaction barriers by a CuPd catalyst to improve the selectivity of CO_2 electroreduction to C_2 products, Chin. J. Catal. 42 (2021) 1500–1508.

[28] Z. Lyu, S. Zhu, L. Xu, et al., Kinetically controlled synthesis of Pd-Cu Janus nanocrystals with enriched surface structures and enhanced catalytic activities toward CO_2 reduction, J. Am. Chem. Soc. 143 (2021) 149–162.

[29] X.Q. Li, G.Y. Duan, J.W. Chen, et al., Regulating electrochemical CO_2RR selectivity at industrial current densities by structuring copper@poly(ionic liquid) interface, Appl. Catal. B Environ. 297 (2021) 120471.

[30] J. Kumar, R. Saxena, Formation of NaCl- and Cu_2O-type oxides of platinum and palladium on carbon and alumina support films, J. Less Common Met. 147 (1989) 59–71.

[31] V. Mukundan, J. Yin, P. Joseph, et al., Nanoalloying and phase transformations during thermal treatment of physical mixtures of Pd and Cu nanoparticles, Sci. Technol. Adv. Mater. 15 (2014) 025002.

[32] A. Raphael Cabral, B. Lehmann, R. Kwitko, et al., Palladium-oxygenated compounds of the Gongo Soco mine, Quadrilátero Ferrífero, central Minas Gerais. Brazil, Mineral. Mag. 65 (2018) 169–179.

[33] A.C. Miller, G.W. Simmons, Copper by XPS, Surf. Sci. Spectra 2 (1993) 55–60.

[34] G. Deroubaix, P. Marcus, X-ray photoelectron spectroscopy analysis of copper and zinc oxides and sulphides, Surf. Interface Anal. 18 (1992) 39–46.

[35] J.P. Espinós, J. Morales, A. Barranco, et al., Interface effects for Cu, CuO, and Cu_2O deposited on SiO_2 and ZrO_2. XPS determination of the valence state of copper in Cu/SiO_2 and Cu/ZrO_2 catalysts, J. Phys. Chem. B 106 (2002) 6921–6929.

[36] J.C. Klein, C.P. Li, D.M. Hercules, et al., Decomposition of copper compounds in X-ray photoelectron spectrometers, Appl. Spectmsc. 38 (2016) 729–734.

[37] J.C. Klein, A. Proctor, D.M. Hercules, et al., X-ray excited Auger intensity ratios for differentiating copper compounds, Anal. Chem. 55 (2002) 2055–2059.

[38] M. Finšgar, X-ray excited Auger Cu $L_3M_{4,5}M_{4,5}$ spectra measured at low take-off angles as a fingerprint for a Cu-organics connection, J. Electron. Spectrosc. Relat. Phenom. 222 (2018) 10–14.

[39] C. Sleigh, A.P. Pijpers, A. Jaspers, et al., On the determination of atomic charge via ESCA including application to organometallics, J. Electron. Spectrosc. Relat. Phenom. 77 (1996) 41–57.

[40] L.S. Kibis, A.I. Stadnichenko, S.V. Koscheev, et al., Highly oxidized palladium nanoparticles comprising Pd^{4+} species: spectroscopic and structural aspects, thermal stability, and reactivity, J. Phys. Chem. C 116 (2012) 19342–19348.

[41] G. Beamson, D. Briggs, High Resolution XPS of Organic Polymers: The Scienta ESCA300 Database, John Wiley & Sons, Chichester, 1992.

[42] P. Aydogan Gokturk, U. Salzner, L. Nyulászi, et al., XPS-evidence for *in-situ* electrochemically-generated carbene formation, Electrochim. Acta 234 (2017) 37–42.

[43] J.K. Sun, Z. Kochovski, W.Y. Zhang, et al., General synthetic route toward highly dispersed metal clusters enabled by poly(ionic liquid)s, J. Am. Chem. Soc. 139 (2017) 8971–8976.

[44] A. Herzog, A. Bergmann, H.S. Jeon J, et al., Operando investigation of Ag-decorated Cu_2O nanocube catalysts with enhanced CO_2 electroreduction toward liquid products, Angew. Chem. Int. Ed. 60 (2021) 7426–7435.

[45] B.A. Steinhoff, S.S. Stahl, Ligand-modulated palladium oxidation catalysis: mechanistic insights into aerobic alcohol oxidation with the $Pd(OAc)_2$/pyridine catalyst system, Org. Lett. 4 (2002) 4179–4181.

[46] A. Wadas, A. Gorczynski, I.A. Rutkowska, et al., Stabilization and activation of Pd nanoparticles for efficient CO_2-reduction: importance of their generation within supramolecular network of tridentate Schiff-base ligands with N,N coordination sites, Electrochim. Acta 388 (2021).

[47] Y. Mun, S. Lee, A. Cho, et al., Cu-Pd alloy nanoparticles as highly selective catalysts for efficient electrochemical reduction of CO_2 to CO, Appl. Catal. B Environ. 246 (2019) 82–88.

[48] Y. Zhao, X. Chang, A.S. Malkani, et al., Speciation of Cu surfaces during the electrochemical CO reduction reaction, J. Am. Chem. Soc. 142 (2020) 9735–9743.

[49] C.T. Williams, A.A. Tolia, H.Y.H. Chan, et al., Surface-enhanced raman spectroscopy as an *in situ* real-time probe of catalytic mechanisms at high gas pressures: the CO–NO reaction on platinum and palladium, J. Catal. 163 (1996) 63–76.

[50] F.P. García de Arquer, C.T. Dinh, A. Ozden, et al., CO_2 electrolysis to multicarbon products at activities greater than 1 A cm^{-2}, Science 367 (2020) 661–666.

Xiao-Qiang Li is presentably a postgraduate student at Beijing Key Laboratory of Ionic Liquids Clean Process, Institute of Process Engineering, Chinese Academy of Sciences. His research interest focuses on the design of organic-inorganic hybrids and application in the catalytic conversion of small molecules.

Bao-Hua Xu is an awardee of the National Natural Science Foundation of Excellent Young Scientists Fund. She completed her Ph.D. degree (2008) at the State Key Laboratory of Coordination Chemistry under the direction of Professor Hong Yan. She did postdoctoral research in Professor Gerhard Erker's group at Münster University (2008–2012). She joined Institute of Process Engineering, Chinese Academy of Sciences as a professor in 2012 and her current scientific interests include designing and regulating the functionality and geometry of ionic liquids/materials, thermo/electro-catalysis application, constructing green catalytic reaction system and process.